

Constructing $\text{CH}_3\text{NH}_3\text{PbI}_3$ and $\text{CH}_3\text{NH}_3\text{PbBr}_3$ Perovskite Thin Film Electronic Structure from Single Crystal Band Structure Measurements

*Fengshuo Zu,^{†,‡} Patrick Amsalem,[†] David A. Egger,^{#,‡} Rongbin Wang,^{†,¶} Christian M.
Wolff,[‡] Honghua Fang,[§] Maria Antonietta Loi,[§] Dieter Neher,[‡] Leeor Kronik,[‡] Steffen
Duhm,[¶] and Norbert Koch^{*†,‡,¶}*

[†]Institut für Physik & IRIS Adlershof, Humboldt-Universität zu Berlin, 12489 Berlin,
Germany

[‡]Helmholtz-Zentrum Berlin für Materialien und Energie GmbH, 12489 Berlin,
Germany

[#]Institute of Theoretical Physics, University of Regensburg, 93040 Regensburg,
Germany

[‡]Department of Materials and Interfaces, Weizmann Institute of Science, Rehovoth
76100, Israel

[¶]Institute of Functional Nano and Soft Materials (FUNSOM), Jiangsu Key Laboratory
for Carbon-based Functional Materials & Devices, Soochow University, Suzhou,
Jiangsu 215123, P. R. China

[‡]Institut für Physik und Astronomie, Universität Potsdam, 14776 Potsdam, Germany

§Photophysics & OptoElectronics, Zernike Institute for Advanced Materials,
University of Groningen, Nijenborgh 4, Groningen, 9747 AG, Netherland

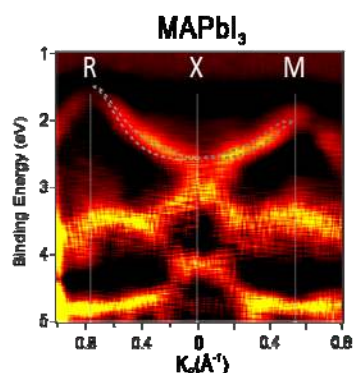
Corresponding Author:

*Email: norbert.koch@physik.hu-berlin.de

Abstract

Photovoltaic cells based on halide perovskites and possessing remarkably high power conversion efficiencies have been reported. To push the development of such devices further, a comprehensive and reliable understanding of their electronic properties is essential, but presently not available. To provide a solid foundation for understanding the electronic properties of polycrystalline thin films, we employ single crystal band structure data from angle-resolved photoemission measurements. For two prototypical perovskites ($\text{CH}_3\text{NH}_3\text{PbBr}_3$ and $\text{CH}_3\text{NH}_3\text{PbI}_3$) we reveal the band dispersion in two high symmetry directions, and identify the global valence band maxima. With these benchmark data, we construct “standard” photoemission spectra from polycrystalline thin film samples and resolve challenges discussed in the literature of determining the valence band onset with high reliability. Within the framework laid out here, the consistency of relating the energy level alignment in perovskite-based photovoltaic and optoelectronic devices with their functional parameters is substantially enhanced.

TOC GRAPHICS



Keywords: single crystal and thin film perovskites, angle-resolved photoemission, low-energy electron diffraction and density functional theory

Tremendous fundamental and application-oriented research efforts are currently devoted to halide perovskites (HaPs), an emerging semiconductor material class that has shown huge promise for highly efficient optoelectronic devices.¹⁻⁷ Despite their success as active material in optoelectronic devices, especially in solar cells,⁸⁻¹⁰ fundamental optoelectronic properties of HaPs are still not comprehensively understood.¹¹⁻¹³ In particular, the electronic band structure is a key for unraveling the intrinsic charge transport properties of a semiconductor, as the effective carrier mass, and thus carrier mobility, is directly related to it. For methylammonium and lead based hybrid organic-inorganic HaPs ($\text{CH}_3\text{NH}_3\text{PbX}_3$ or MAPbX_3 , $X = \text{Cl, Br, I}$), several theoretical studies, performed within the framework of density functional theory (DFT) or many-body perturbation theory, have investigated the band structure.^{2, 14-22} In these studies, the hole effective mass (m_h^*) of MAPbI_3 was predicted to be in the range of $0.2 m_0$ ^{14, 23} to $0.5 m_0$,¹⁷ (where m_0 is the free electron mass), with the precise value depending on details of the crystal structure, inclusion of spin-orbit coupling, the directions probed in reciprocal space (k -space), and the level of theory.

Experimentally, the electronic properties of polycrystalline thin films of HaPs have been studied with photoelectron spectroscopy (PES), mostly to investigate the energy level alignment at device-related interfaces.²⁴⁻³⁰ Only few experimental studies have probed the band structure of single-crystalline hybrid HaPs directly using angle-resolved PES (ARPES),³¹⁻³⁵ where the focus so far was on MAPbBr_3 , with the exception of the reports by Lee et al.³⁴ and Yang et al.³⁵ Knowledge of the surface structure is likewise important, as the electronic structure, and therefore charge transport properties, of HaPs are a consequence of the structure. For example, the bulk structure of MAPbBr_3 and MAPbI_3 undergoes a transition from tetragonal to cubic as the temperature increases, and for MAPbI_3 the coexistence of both structures around room temperature (RT) was reported.³⁶ For the cubic phase of MAPbI_3 , m_h^* was estimated from ARPES to be in the range of $0.24 m_0$ to $0.35 m_0$ for the M and X points

of the Brillouin zone (BZ).³⁵ However, no value for the global valence band maximum (VBM) at the R point, which has the lowest binding energy (BE) and thus is most relevant for carrier transport, has been reported for MAPbI₃.

While knowing the hole effective masses contributes to a better understanding of the intrinsic transport properties of HaPs, it is likewise important to link band structure data obtained on single crystals to the electronic properties of thin films that are applied in devices. One key parameter is the position of the VBM with respect to the Fermi level (E_F), as this allows the assessment of the doping level of the materials, as well as – in conjunction with work function determination – the ionization energy (IE). Reliably known IE values of HaPs help in guiding the selection of appropriate charge transport or blocking materials in multilayer devices. However, it transpired that the conventional way of determining the VBM, by linear extrapolation of the lowest BE PES feature on a linear intensity scale, does not return reliable values.^{11, 29, 37-38} Instead, it was proposed that due to an “unusually low” density of states (DOS) at the VBM of numerous perovskites, the extrapolation should be done for PES data plotted on a logarithmic scale.²⁹ The low intensity tail of the DOS was explained via wide and possibly nonparabolic band dispersion.²¹ It should, however, be possible to derive the reasoning for using a logarithmic PES intensity scale to extract VBM values directly from experimental band structure data, in order to ascertain the consistency of experimentally determined key parameters such as the band structure and the DOS.

Here, we present a combined low-energy electron diffraction (LEED) and ARPES study of MAPbI₃ and MAPbBr₃ single crystals, complemented by periodic-boundary-conditions hybrid functional DFT calculations that account for spin-orbit coupling, with further *a posteriori* corrections. For these HaPs, the surface orientation, lattice parameters, and crystal symmetry group were determined by LEED, and the electronic band structure was investigated along high symmetry momentum directions by ARPES. We resolve strongly dispersive features in the band structure of the HaPs, particularly along the X - R direction, thus indeed reaching the global VBM. From the band structure, we assess that the VBM can be reliably retrieved with the conventional method used in

semiconductor physics of extrapolation on a linear PES intensity scale, if sample and experimental geometry allow reaching the appropriate point of the Brillouin zone. From our benchmark quality ARPES data, we then construct conventional PES spectra of polycrystalline thin film samples, and provide the underlying reasoning why the logarithmic scale provides a better approximation for VBM values. Based on this understanding of thin film spectra from single crystal experimental band structures, a solid foundation for obtaining highly reliable information on the electronic structure of HaP thin films is provided.

Surface Structure

The first bulk and surface Brillouin zones (BZ) of a cubic lattice are displayed in Figure 1(a). The LEED pattern of the MAPbBr₃ single crystal surface at RT, shown in Figure 1(b), exhibits a square diffraction pattern, as expected for the (001) surface. The lattice parameters estimated from this LEED pattern are $a_{LEED} = b_{LEED} = 5.72 \pm 0.10$ Å, in good agreement with the lattice parameters of the cubic structure ($a = b = c = 5.90$ Å, space group Pm3m).³⁹ It is noted that the crystal undergoes a structural transition to the β phase of the tetragonal lattice upon lowering the temperature, which is shown and discussed in Figure S1 of the supplementary information (SI).

The LEED patterns obtained from our MAPbI₃ single crystal (001) surface at RT exhibit a pattern that confirms the coexistence of cubic and tetragonal structures, as pointed out earlier.^{35-36, 40} The LEED pattern taken with an electron energy of 21 eV [Figure 1(c)] features sets of bright and dim spots, whereas the dim spots are barely present in the LEED pattern taken with 33 eV primary energy, as shown in Figure 1(d). The lattice parameter determined from the dim spots in Figure 1(c) is $a^T = 7.96 \pm 0.16$ Å, which corresponds within 10% to that of the (001) surface of the tetragonal phase (8.87 Å).³⁹ The lattice parameter determined from the sets of bright spots at both electron energies is $a^C = 6.02 \pm 0.11$ Å, which is in satisfactory agreement with the known lattice parameter of the pseudocubic phase (6.30 Å)⁴⁰, and also in line with a LEED study. Given the higher intensity LEED spots corresponding to the cubic phase, we suggest that it is predominantly abundant at the surface, as unambiguously confirmed by ARPES results shown below.

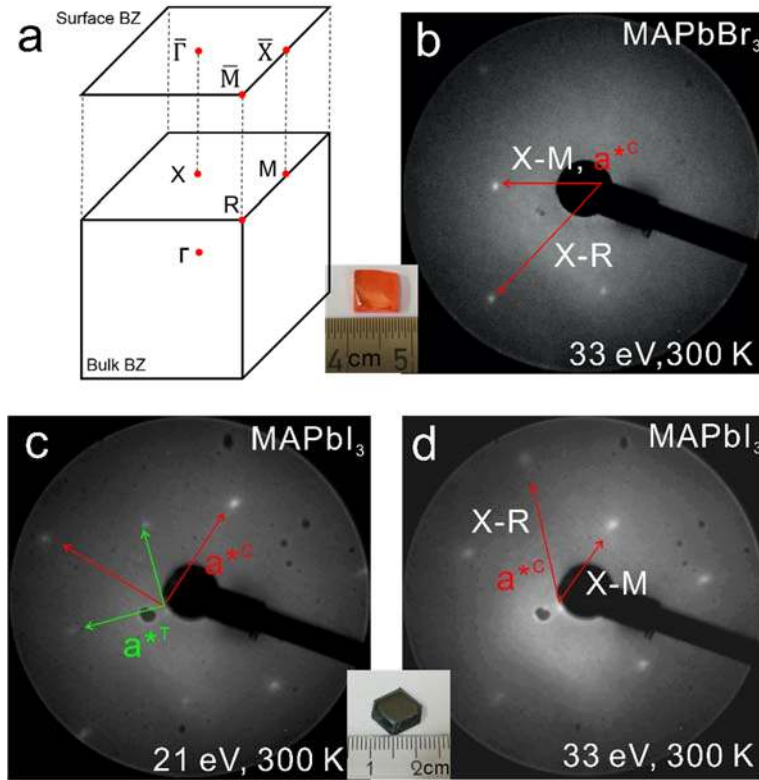


Figure 1. Single crystal surface structure. (a) The first bulk Brillouin zone (BZ) and surface Brillouin zone (SBZ) of a cubic lattice, with an inset showing a photograph of one of the MAPbBr₃ single crystals. (b): LEED pattern of the (001) plane of a MAPbBr₃ single crystal, at an electron energy of 33 eV at 300 K. The reciprocal lattice parameter a^{*C} refer to the cubic phase. ARPES measurements were performed along the X - M and X - R directions [highlighted with red lines in (b)]. (c) and (d): LEED patterns of the (001) plane of a MAPbI₃ single crystal at 300 K, at an electron energy of 21 eV and 33 eV, respectively, with the inset showing a photograph of a MAPbI₃ single crystal. The reciprocal lattice parameters a^{*C} and a^{*T} refer to the cubic and tetragonal phases, respectively. ARPES measurements were performed along the X - M and X - R directions [highlighted with red lines in (d)].

Single Crystal Electronic Band Structure

ARPES measurements were conducted at RT along high symmetry directions, as indicated in the LEED patterns shown in Figure 1(b) and (d). For MAPbBr₃, the as-

obtained ARPES spectra as a function of k_{\parallel} (the electron wave vector component parallel to the sample surface, determined according to the relation:⁴¹ $\hbar k_{\parallel} = \sqrt{2m_0 E_{kin}} \times \sin\theta$, where E_{kin} is the measured kinetic energy of the photoelectrons and θ the electron emission angle with respect to the surface normal) are shown in Figure S2 of the SI. For improved visualization of electronic bands and their dispersion, the ARPES spectra were analyzed using the 2D curvature method,⁴² as displayed in Figure 2. These treated ARPES data appear sharper, which assists in tracking the k -dependent peak positions and allows for a more straightforward comparison with the DFT-calculated band structure.

Because the electron wave vector component perpendicular to the surface (k_{\perp}) is not conserved in ARPES experiments and the k_{\perp} -resolution depends on the photoelectron kinetic energy, we need to consider whether our experimental conditions allow measurements within the so-called band structure regime (i.e., information about the k_{\perp} position within the BZ is retained) or whether they only provide the one-dimensional density-of-states (1-DOS).⁴³⁻⁴⁴ In the latter case, our measurement directions would be along $\bar{\Gamma}-\bar{M}$ and $\bar{\Gamma}-\bar{X}$ of the surface BZ [see Figure 1(a)]. According to the criterion for the band structure regime derived by Strocov,⁴³ the photoelectron escape length λ should be comparable to or longer than the crystal lattice parameter along the surface normal. Our data (λ in the range of 3-20 Å⁴⁵⁻⁴⁶ and $a^c \approx 6$ Å) could be in that regime but could also be borderline. However, we can use our DFT calculations (see Methods section for details) to assign the probed directions more accurately. For both perovskite crystals, we find wide dispersion of the top valence bands along the two principal directions (inclined by 45° as indicated in Figure 1). This observation can be matched best by assuming the $X-M$ and $X-R$ momentum directions of the bulk BZ according to the calculated band structures (Figures S3 and S4 of the SI), as dispersion along $\bar{\Gamma}-\bar{X}$ is minimal. In fact, by overlaying the calculated bands along the $X-M$ and $X-R$ directions with the photoemission data, we find good overall agreement between theory and experiment, as seen in Figs. 2 (a), (b), (d), and (e). For example, in experiment the bandwidths found for MAPbBr₃ amount to 1.3 eV and 0.7

eV along the X - R and X - M directions, respectively, comparing nicely with the calculated bandwidths (1.5 eV and 0.8 eV for these two directions). One more observation leads us to conclude that we do indeed capture the global VBM at R (as found in calculations, see Figs. S3 and S4), which is the fact that the BE of the valence band top in Figure 2(b) and (e) coincides with the valence band onset found when plotting our data on a logarithmic intensity scale (see Discussion section and Figure 3 below), as suggested in previous work.²⁹

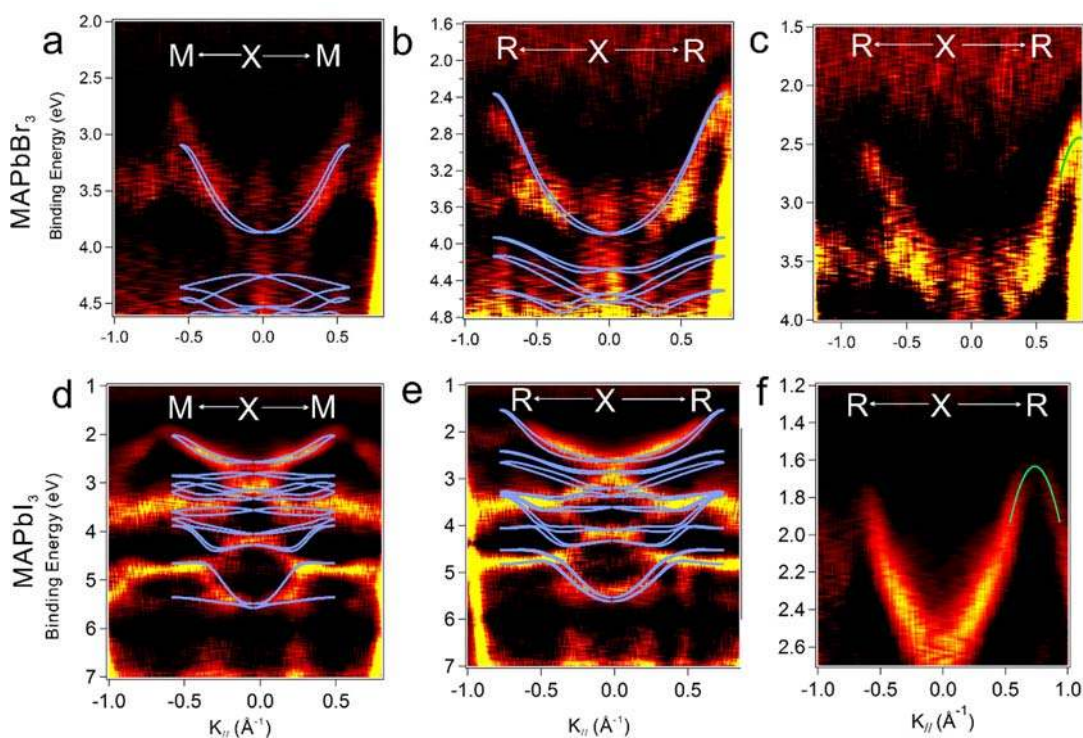


Figure 2. ARPES k -space 2D curvature band maps. Top row: Of a MAPbBr₃ single crystal along the (a) X - M and (b) X - R high symmetry directions. Bottom row: Of a MAPbI₃ single crystal along the (c) X - M and (d) X - R high symmetry directions. In all plots, corresponding DFT calculated bands are shown in light blue lines (shifted in energy to match experimental band positions). A zoom into the topmost valence band along the X - R direction is given in (c) for MAPbBr₃ and in (f) for MAPbI₃. Fitting the valence band edge regions with parabolic curves (green lines) yields a hole effective mass near R of $\sim 0.25 \pm 0.05 m_0$ for MAPbBr₃ and $\sim 0.50 \pm 0.10 m_0$ for MAPbI₃. Corresponding fits for the X - M direction are shown in Figure S5 of the SI.

According to the above assignment of directions, the periodicity of the ARPES spectra from MAPbBr₃ in Figure 2(a) allows the determination of a lattice parameter, $a_{ARPES} = 5.56 \pm 0.29 \text{ \AA}$, which matches the conclusions from LEED analysis regarding the presence of the cubic phase (see above). Furthermore, one key parameter for charge transport properties of hybrid HaP semiconductors is the hole effective mass, m_h^* , which we determine for MAPbBr₃ to be $0.25 \pm 0.08 m_0$ for the near R (in the X - R direction), by applying a parabolic fit to the VBM, as illustrated in Figure 2 (c), and $0.30 \pm 0.15 m_0$ near M [Figure S5(a) in the SI].

The as-measured ARPES spectra for MAPbI₃ are shown in Figs. S2(c) and (d), with the corresponding spectra processed with the 2D curvature method for better visualization given in Figs. 2(d) and (e). The assignment of band dispersion directions was performed as just described above. Notable contributions of the tetragonal structure to the photoemission spectra are not apparent, as in this structure the top of the valence band would appear along Γ - Z (see Figure S6), where we do not observe intensity. The lattice parameter determined from the periodicity along X - M amounts to $5.97 \pm 0.18 \text{ \AA}$, corresponding very well with the lattice parameter of the cubic phase a^C above. As for the Br-based HaP, also for MAPbI₃ it can be clearly seen that the VBM is located at R , consistent with the theoretical results by Brivio et al.²¹ and our own for the cubic phase of MAPbI₃. The topmost valence bandwidths are 0.6 eV (X - M) and 1.0 eV (X - R), again in excellent agreement with the calculated ones for the cubic structure (0.6 eV and 1.1 eV, respectively). For some of the higher BE bands, differences between ARPES and DFT are found, most notably we do not clearly observe the calculated four bands just below the top valence bands in the experimental data (as can be seen best in the curvature spectra). The reasons for this deviation are unknown at this point, and are possibly related to matrix element effects given the polarization of the incident light, which can potentially modify the measured photoelectron intensity.⁴⁷⁻⁴⁸ There might also be a structural difference between the sample surface and bulk, as the cubic structure could be confined to the near-surface region in experiment, while calculations were performed for an infinite bulk. Identifying the origin of this observation should be

the subject of further studies. We note that, remarkably, features related to the tetragonal phase [its presence confirmed by the lower intensity LEED spots in Figure 1(c)] are not apparent in the ARPES spectra. This is consistent with the predominant intensity of the diffraction spots from the cubic phase, as the final state in photoemission corresponds to time-reversed LEED states within the one-step theory of photoemission.⁴⁹ We also performed a parabolic fit of the VBM at R (M), as depicted in Figure 2(f) [Figure S5(b) in the SI], to evaluate m_h^* . We find rather small values of $0.18 \pm 0.06 m_0$ at M (along X - M) and $0.50 \pm 0.10 m_0$ near R (along the X - R momentum direction). These values are in good agreement with theoretically predicted ones.^{14, 23} While m_h^* at R for MAPbI₃ was not experimentally determined in Ref.³⁵, it was estimated to be $0.4 m_0$, i.e., reasonably close to our result.

Based on these m_h^* values, we conclude on lower limit hole mobilities in the range of several tens of cm^2/Vs , in agreement with Yang et al.³⁵ While a theoretical approach⁵⁰ based on the Kane model estimated the hole mobility (μ_h) for pseudocubic MAPbI₃ to be $800\text{-}1500 \text{ cm}^2/\text{V}\cdot\text{s}$, depending on charge carrier concentration, experimentally determined mobilities are 1-2 orders of magnitude lower.¹³ We note that such discrepancy between small effective mass and relatively low mobility has been recently brought up in the discussion of hybrid organic-inorganic lead halide perovskite electronic properties.^{11-12, 51-54} To explain the lower than expected mobility, it was proposed that transport properties are not a result of bare carriers (i.e., electrons or holes) but, because of efficient Coulomb screening and soft lattices, resembling large polarons (i.e., exhibiting radii extending over a few unit cells) bands with potentially heavy masses.^{51-53, 55-56} While polaron formation certainly impacts charge transport, we do not observe polaronic effects in the band structure, owing to the fact that photoemission typically occurs on the fs time-scale, while large-polaron formation is expected to take place within $\sim 10^2$ fs.⁵¹ It would therefore be of much interest to investigate this further, e.g., by performing time-resolved two-photon ARPES measurements on such materials.

From Single Crystals to Thin Films

With the detailed knowledge of the single crystal band structures of the two HaPs, we can unambiguously understand the electronic structure of polycrystalline films and

resolve the challenges of reliable valence band onset determination. Using MAPbI₃ as an example, we plot energy distribution curves (EDCs), i.e., photoemission intensity as function of electron BE for defined emission angles at different $k_{//}$ values (full range shown in Figure S7 in the SI). Selected “cuts” through the band structure between X - M and X - R are shown on a linear intensity scale in Figs. 3(a) and (b) (the directions of the cuts through the band structure are marked in the respective figure insets). As indicated in the figures, for each direction of $k_{//}$ one can find the valence band (VB) onset well by extrapolation of the leading edge towards the background. However, due to the wide dispersion of the topmost valence bands, the onset varies substantially with $k_{//}$. The respective values are plotted in Figure 3(c). As expected, they follow the valence band dispersion, with a clear highest binding energy VB onset at X ($\bar{\Gamma}$) [Figure 3(c)] and the lowest BE onset of 1.41 eV at R . For comparison, and as suggested earlier,²⁹ we also plot the same data on a logarithmic intensity scale, again determining the VB onset from the intersection with background (Figure S8). In contrast to the data from linear scale, the $k_{//}$ -dependent VB onsets determined from the semi-log plot do not reproduce the dispersion curve. There is only little variation with $k_{//}$, but the lowest binding energy VB onset is also found at R with 1.30 eV. Therefore, the lowest binding energy VB onset is in the range of 1.30 eV – 1.41 eV, where indeed the global VBM is located (Figure S4 in the SI), depending on determination procedure. Possibly, the nearly-absent $k_{//}$ -dependence of the onset determined on logarithmic scale is due to very low photoemission intensity originating from surface patches in the tetragonal phase, whose global VBM is expected at the BZ center. Additionally, that low intensity aside from R may arise from the photoelectrons being scattered by adsorbates on the surface, which has been previously reported to have final-state diffraction effects in photoemission experiments.⁵⁷⁻⁵⁹

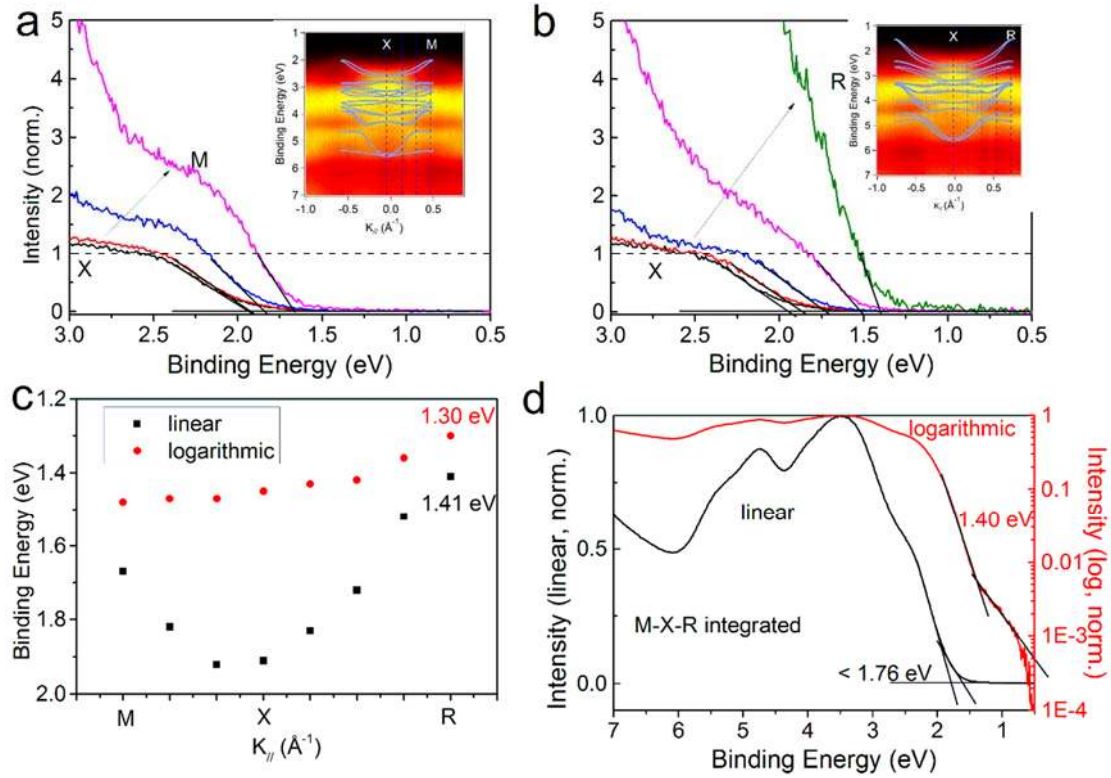


Figure 3. Energy distribution curves (EDCs) and VBM determination for MAPbI₃.

(a) and (b): EDCs at selected k -values along the X - M and X - R directions, respectively. The corresponding k values for the EDCs are indicated by the vertical dashed lines in the ARPES k -space maps [insets in (a) and (b)]. Spectra are normalized at the corresponding top valence band peaks positions (shown in Figure S7) in order to better illustrate the k -dependence of the valence band onsets. (c) Valence band maximum determination from the EDCs plotted in (a) and (b), using linear and logarithmic intensity scales for selected k values along M - X - R . (d) Simulated MAPbI₃ polycrystalline thin film UPS spectrum, obtained by summation of all EDCs from (a) and (b), shown on linear and logarithmic scales to highlight the variation in VBM determination. Fully analogous data for MAPbBr₃ are given in Figure S9 of the SI.

To relate the single crystal electronic structure to those of polycrystalline MAPbI₃ thin films, we integrated the individual single crystal EDCs (from Figure S7) over the full BZ. The resulting “artificial” thin film spectrum is shown in Figure 3(d), on both linear and logarithmic intensity scales. It can be clearly seen that the VB onset evaluated

from extrapolation on the linear scale is very subjective, and readily overestimates the VB onset BE. From the semi-log plot, however, the VB onset is found at 1.40 eV, which is virtually identical to the global VBM found from the appropriate ARPES spectrum taken at R [Figure 3(c)]. Fully analogous data analysis for MAPbBr₃ are shown in Figure S9 and provide essentially identical insight. Therefore, as for standard PES measurements on polycrystalline HaP films, using the semi-log plot is indeed more useful for estimating the VB onset, in agreement with Endres et al.²⁹

To evaluate the reliability of applying semi-log plots for HaP thin films, two different MAPbI₃ polycrystalline thin films measured using two different photoemission systems are compared in Figure 4. The overall valence band features are very similar, with one apparent peak at 3.7 eV BE for both films (linear intensity scale). Similar to the observations made for the "artificial" thin film spectrum of Figure 3 (d), the logarithmic-scaled intensity plots for both films lead to VB onset values that are close to the global VBM. Note that the VB onset position of MAPbI₃ films varies with the density of surface states⁶⁰ and the history of exposure to water and oxygen⁶¹, i.e., these values are sample-specific and not an intrinsic material constant. In contrast, the linear scale plots give rise to overestimated VB onset BE. It is worth pointing out that the signal-to-background level differs by a factor of four between the two spectra shown in Figure 4; however, this impacts the onset determined in the semi-log plot by only ca. 40 meV, as demonstrated and discussed in the SI (Figure S10). Similarly, we show in Figure S11 that even ca. twofold variation of the typical experimental broadening changes the VB onset determined on logarithmic intensity scale by only 50 meV. However, it is important to note that HaPs tend to form textured thin films,^{38, 60, 62} with preferential surface orientation to some degree. As a consequence, the accurate position of the VB onset may be missed in standard (and normal-emission) PES experiments, as the relative contribution of intensity from the global VBM may vary considerably [see, e.g., Figure 3(c)]. Furthermore, a careful consideration of the presence and abundance of gap-states⁶³ as well as non-monochromated light source satellites is advisable when studying HaP thin films with PES.

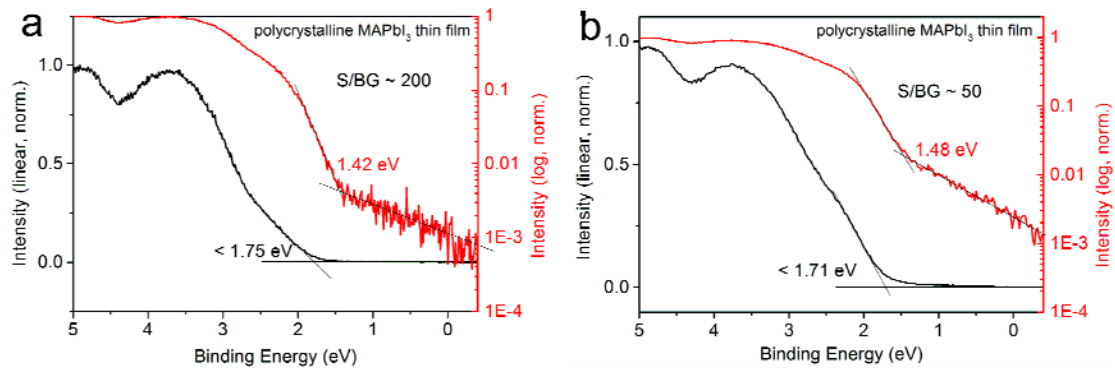


Figure 4. UPS spectra of two different MAPbI₃ polycrystalline thin films measured using (a) SPECS Phoibos 150 analyzer (same system as ARPES) and (b) SPECS Phoibos 100 analyzer; the signal-to-background ratio (S/BG) of the spectra differs by a factor of four (see Figure S10 for details).

The electronic band structure of MAPbBr₃ and MAPbI₃ single crystals with cubic surfaces was determined along high symmetry directions by combining LEED and ARPES measurements. In conjunction with DFT calculations, we identified the widely dispersing (more than 1 eV) top valence bands, as well as the global valence band maxima at the *R* point for both prototypical HaPs, and determined the hole effective masses there to be $\sim 0.25 m_0$ (MAPbBr₃) and $\sim 0.50 m_0$ (MAPbI₃). From the experimental single crystal band structures, the electronic spectra of polycrystalline thin films were constructed, revealing that the comparably small contribution from the global VBM at *R* to area- and angle-averaged spectra compromises a straightforward valence band onset determination of HaPs. This problem is further aggravated by the energetic proximity of many weakly dispersing bands close to the top valence bands. As suggested earlier,²⁹ using a logarithmic intensity scale to determine the VB onset is thus preferable (with a remaining fundamental uncertainty of ca. 50 meV, mostly underestimating the onset BE), but all experimental parameters, such as instrumental limitations and sample gap states, must still be carefully considered. It is particularly important to know the surface structure of thin films when discussing HaP electronic properties in relation to energy levels in devices. We expect that the fundamental insights on thin film electronic spectra, derived from benchmark single crystal band

structures, will enhance progress in device performance, as superior consistency of correlating electronic level alignment and device characteristics is readily enabled.

Experimental Methods

Perovskite thin films and single crystals preparation. Large-sized (millimeter) single crystals of MAPbBr₃ and MAPbI₃, with high crystalline quality, were grown from a saturated solution using a seed-induced nucleation method.³⁹ The crystals were cleaved with a scalpel in a N₂-filled glove box before photoemission measurements and transferred to the UHV system without air exposure. The MAPbI₃ thin films were prepared in a N₂-filled glove box using one-step spin-coating method²⁵ and transferred to the UHV system without air exposure.

Low-energy electron diffraction (LEED), ultraviolet photoelectron spectroscopy (UPS) and angle-resolved PES (ARPES). LEED and ARPES experiments were performed in an ultrahigh vacuum (UHV) system consisting of two sample preparation and analysis chambers (all at base pressure of 2×10^{-10} mbar), as well as a fast load-lock (base pressure of 2×10^{-7} mbar).⁶⁴ LEED experiments were conducted using a Micro-Channel-Plate LEED (OCI BDL800IR-MCP). All LEED patterns presented were corrected from distortion following the procedure described by Mom et al.⁶⁵ ARPES measurements were carried out using plane-grating monochromatized He I α radiation (21.22 eV, SPECS UVS300) and PHOIBOS 150 analyzer equipped with monochrome CCD detector (1376×1040 pixels). A Au (111) surface was used to calibrate the system and the energy resolution was set to 80 meV. Because the acceptance angle of $\pm 12^\circ$ is not enough to cover the first BZ, ARPES measurements at three emission angles (0° , -20° and $+20^\circ$) were conducted sequentially for each momentum direction. Consequently, the presented ARPES spectra over a wide range of k -space consist of three sub-ARPES measurements. All measurements were performed at RT (300 K).

UPS measurements on polycrystalline MAPbI₃ thin films were performed using above mentioned ARPES setups, as well as using a setup equipped with a SPECS Phoibos 100 analyzer combining with standard helium discharge lamp (21.22 eV).

Valence band onset determination. Graphical determination of VB onsets using linear and semi-log extrapolation methods was done by determining the intersection point between the background line and a tangent line taken at the inflection point of the top

valence band.

All valence band spectra were first normalized to the maximum peak intensity before applying the semi-log extrapolation method.

Density functional theory. DFT calculations were performed using the VASP plane-wave code,⁶⁶ using the HSE exchange-correlations functional⁶⁷ including spin-orbit coupling, and ‘normal’ PAW potentials (treating the *5d* electrons of Pb explicitly) with a plane-wave kinetic energy cutoff of 400 eV. To allow for interpretation of the experimental data despite the remaining deficiencies of our theoretical approach, we performed an *a posteriori* correction by “stretching” the eigenvalue spectrum according to the values reported in our previous study.²⁹ Cubic unit-cells of MAPbI₃ and MAPbBr₃ with previously calculated lattice constants⁶⁸ and a 4x4x4 Γ -centered *k*-point grid were used for self-consistently calculating the charge-density. Subsequent band-structure calculations were performed non-self-consistently using an equally-spaced *k*-grid of 50 points between the high-symmetry points of the Brillouin zone.

ASSOCIATED CONTENT

Supporting information

The Supporting Information is available free of charge on the ACS Publication website. LEED pattern of the MAPbBr₃ single crystal; ARPES *k*-space maps of the MAPbBr₃ single crystal; DFT-calculated valence band structure of MAPbI₃ and MAPbBr₃ at cubic phase; Top valence band for MAPbI₃ and MAPbBr₃ along *X-M* direction; DFT-calculated valence band structure of MAPbI₃ at tetragonal phase; EDCs of the MAPbI₃ single crystal in linear and logarithmic intensity scale; EDCs and VBM determination for MAPbBr₃ single crystal; A simulated Gaussian peak plotted in linear and logarithmic scale; Effect of experimental broadening in the valence band edge region (PDF)

AUTHOR INFORMATION

Corresponding Author

*Email: norbert.koch@physik.hu-berlin.de

Notes

The authors declare no competing financial interests.

ACKNOWLEDGMENTS

We would like to thank Mr. Tianshu Zhai for experimental support during ARPES measurements and Prof. Nobuo Ueno and Prof. Satoshi Kera for helpful discussion. This work was supported by the Helmholtz Energy Alliance "Hybrid Photovoltaics", the Joint Graduate School HyPerCells of the University of Potsdam and the Helmholtz Zentrum Berlin, the DFG (SFB951), the 111 Project of the Chinese State Administration of Foreign Experts Affairs, the Collaborative Innovation Center of Suzhou Nano Science & Technology (NANO-CIC), the Sustainability and Energy Research Initiative (SAERI) at the Weizmann Institute, and the Minerva Foundation. P. A. acknowledges the DFG (AM 419/1-1) for financial support.

REFERENCES

- (1) Jung, H. S.; Park, N. G. Perovskite Solar Cells: from Materials to Devices. *Small* **2015**, *11*, 10-25.
- (2) Berry, J.; Buonassisi, T.; Egger, D. A.; Hodes, G.; Kronik, L.; Loo, Y. L.; Lubomirsky, I.; Marder, S. R.; Mastai, Y.; Miller, J. S.; Mitzi, D. B.; Paz, Y.; Rappe, A. M.; Riess, I.; Rybtchinski, B.; Stafsudd, O.; Stevanovic, V.; Toney, M. F.; Zitoun, D.; Kahn, A.; Ginley, D.; Cahen, D. Hybrid Organic-Inorganic Perovskites (HOIPs): Opportunities and Challenges. *Adv. Mater.* **2015**, *27*, 5102-5112.
- (3) Wang, N.; Cheng, L.; Ge, R.; Zhang, S.; Miao, Y.; Zou, W.; Yi, C.; Sun, Y.; Cao, Y.; Yang, R.; Wei, Y.; Guo, Q.; Ke, Y.; Yu, M.; Jin, Y.; Liu, Y.; Ding, Q.; Di, D.; Yang, L.; Xing, G.; Tian, H.; Jin, C.; Gao, F.; Friend, R. H.; Wang, J.; Huang, W. Perovskite Light-Emitting Diodes based on Solution-Processed Self-Organized Multiple Quantum Wells. *Nat. Photon.* **2016**, *10*, 699-704.
- (4) Tan, Z. K.; Moghaddam, R. S.; Lai, M. L.; Docampo, P.; Higler, R.; Deschler, F.; Price, M.; Sadhanala, A.; Pazos, L. M.; Credgington, D.; Hanusch, F.; Bein, T.; Snaith, H. J.; Friend, R. H. Bright Light-Emitting Diodes based on Organometal Halide Perovskite. *Nat. Nanotechnol.* **2014**, *9*, 687-692.
- (5) Pazos-Outón, L. M.; Szumilo, M.; Lamboll, R.; Richter, J. M.; Crespo-Quesada, M.; Abdi-Jalebi, M.; Beeson, H. J.; Vrućinić, M.; Alsari, M.; Snaith, H. J.; Ehrler, B.; Friend, R. H.; Deschler, F. Photon Recycling in Lead Iodide Perovskite Solar Cells. *Science* **2016**, *351*, 1430-1433.
- (6) Yang, X.; Zhang, X.; Deng, J.; Chu, Z.; Jiang, Q.; Meng, J.; Wang, P.; Zhang, L.; Yin, Z.; You, J. Efficient Green Light-Emitting Diodes based on Quasi-Two-Dimensional Composition and Phase Engineered Perovskite with Surface Passivation. *Nat. Commun.* **2018**, *9*, 570.
- (7) Brenner, T. M.; Egger, D. A.; Kronik, L.; Hodes, G.; Cahen, D. Hybrid Organic—Inorganic Perovskites: Low-Cost Semiconductors with Intriguing Charge-Transport Properties. *Nat. Rev. Mater.* **2016**, *1*, 15007.
- (8) Tan, H.; Jain, A.; Voznyy, O.; Lan, X.; García de Arquer, F. P.; Fan, J. Z.; Quintero-Bermudez, R.; Yuan, M.; Zhang, B.; Zhao, Y.; Fan, F.; Li, P.; Quan, L. N.; Zhao, Y.; Lu, Z.-H.; Yang, Z.; Hoogland, S.; Sargent, E. H. Efficient and Stable Solution-Processed Planar Perovskite Solar

- Cells via Contact Passivation. *Science* **2017**, *355*, 722-726.
- (9) Li, X.; Bi, D.; Yi, C.; Décoppet, J.-D.; Luo, J.; Zakeeruddin, S. M.; Hagfeldt, A.; Grätzel, M. A Vacuum Flash-Assisted Solution Process for High-Efficiency Large-Area Perovskite Solar Cells. *Science* **2016**, *353*, 58-62.
- (10) Rong, Y.; Hou, X.; Hu, Y.; Mei, A.; Liu, L.; Wang, P.; Han, H. Synergy of Ammonium Chloride and Moisture on Perovskite Crystallization for Efficient Printable Mesoscopic Solar Cells. *Nat. Commun.* **2017**, *8*, 14555.
- (11) Egger, D. A.; Bera, A.; Cahen, D.; Hodes, G.; Kirchartz, T.; Kronik, L.; Lovrincic, R.; Rappe, A. M.; Reichman, D. R.; Yaffe, O. What Remains Unexplained about the Properties of Halide Perovskites? *Adv. Mater.* **2018**, *30*, 1800691.
- (12) Brenner, T. M.; Egger, D. A.; Rappe, A. M.; Kronik, L.; Hodes, G.; Cahen, D. Are Mobilities in Hybrid Organic-Inorganic Halide Perovskites Actually "High"? *J. Phys. Chem. Lett.* **2015**, *6*, 4754-4757.
- (13) Herz, L. M. Charge-Carrier Mobilities in Metal Halide Perovskites: Fundamental Mechanisms and Limits. *ACS Energy Lett.* **2017**, *2*, 1539-1548.
- (14) Menéndez-Proupin, E.; Palacios, P.; Wahnón, P.; Conesa, J. C. Self-Consistent Relativistic Band Structure of the CH₃NH₃PbI₃ Perovskite. *Phys. Rev. B* **2014**, *90*, 045207.
- (15) Gao, W.; Gao, X.; Abtey, T. A.; Sun, Y.-Y.; Zhang, S.; Zhang, P. Quasiparticle Band Gap of Organic-Inorganic Hybrid Perovskites: Crystal Structure, Spin-Orbit Coupling, and Self-Energy Effects. *Physical Review B* **2016**, *93*, 085202.
- (16) Even, J.; Pedesseau, L.; Katan, C.; Kepenekian, M.; Lauret, J.-S.; Saponi, D.; Deleporte, E. Solid-State Physics Perspective on Hybrid Perovskite Semiconductors. *J. Phys. Chem. C* **2015**, *119*, 10161-10177.
- (17) Umari, P.; Mosconi, E.; De Angelis, F. Relativistic GW Calculations on CH₃NH₃PbI₃ and CH₃NH₃SnI₃ Perovskites for Solar Cell Applications. *Sci. Rep.* **2014**, *4*, 4467.
- (18) Park, J. S.; Choi, S.; Yan, Y.; Yang, Y.; Luther, J. M.; Wei, S. H.; Parilla, P.; Zhu, K. Electronic Structure and Optical Properties of alpha-CH₃NH₃PbBr₃ Perovskite Single Crystal. *J. Phys. Chem. Lett.* **2015**, *6*, 4304-4308.
- (19) Y. H. Chang; C. H. Park; Matsuishi, K. First-Principles Study of the Structural and the Electronic Properties of the Lead-Halide-Based Inorganic-Organic perovskites

- (CH₃NH₃)PbX₃ and CsPbX₃ (X = Cl, Br, I). *J. Korean Phy. Soc.* **2004**, *44*, 889-893.
- (20) Filip, M. R.; Eperon, G. E.; Snaith, H. J.; Giustino, F. Steric Engineering of Metal-Halide Perovskites with Tunable Optical Band Gaps. *Nat. Commun.* **2014**, *5*, 5757.
- (21) Brivio, F.; Butler, K. T.; Walsh, A.; van Schilfgaarde, M. Relativistic Quasiparticle Self-Consistent Electronic Structure of Hybrid Halide Perovskite Photovoltaic Absorbers. *Phys. Rev. B* **2014**, *89*, 155204.
- (22) Jishi, R. A.; Ta, O. B.; Sharif, A. A. Modeling of Lead Halide Perovskites for Photovoltaic Applications. *J. Phys. Chem. C* **2014**, *118*, 28344-28349.
- (23) Yu, Z. G. Effective-Mass Model and Magneto-Optical Properties in Hybrid Perovskites. *Sci. Rep.* **2016**, *6*, 28576.
- (24) Schulz, P.; Whittaker-Brooks, L. L.; MacLeod, B. A.; Olson, D. C.; Loo, Y.-L.; Kahn, A. Electronic Level Alignment in Inverted Organometal Perovskite Solar Cells. *Adv. Mater. Interfaces* **2015**, *2*, 1400532.
- (25) Wolff, C. M.; Zu, F.; Paulke, A.; Toro, L. P.; Koch, N.; Neher, D. Reduced Interface-Mediated Recombination for High Open-Circuit Voltages in CH₃NH₃PbI₃ Solar Cells. *Adv. Mater.* **2017**, 1700159-n/a.
- (26) Zu, F.; Amsalem, P.; Ralairisoa, M.; Schultz, T.; Schlesinger, R.; Koch, N. Surface State Density Determines the Energy Level Alignment at Hybrid Perovskite/Electron Acceptors Interfaces. *ACS Appl. Mater. Interfaces* **2017**, *9*, 41546-41552.
- (27) Shin, D.; Kang, D.; Jeong, J.; Park, S.; Kim, M.; Lee, H.; Yi, Y. Unraveling the Charge Extraction Mechanism of Perovskite Solar Cells Fabricated with Two-Step Spin Coating: Interfacial Energetics between Methylammonium Lead Iodide and C60. *J. Phys. Chem. Lett.* **2017**, *8*, 5423-5429.
- (28) Hawash, Z.; Raga, S. R.; Son, D. Y.; Ono, L. K.; Park, N. G.; Qi, Y. Interfacial Modification of Perovskite Solar Cells using an Ultrathin MAI Layer Leads to Enhanced Energy Level Alignment, Efficiencies, and Reproducibility. *J. Phys. Chem. Lett.* **2017**, *8*, 3947-3953.
- (29) Endres, J.; Egger, D. A.; Kulbak, M.; Kerner, R. A.; Zhao, L.; Silver, S. H.; Hodes, G.; Rand, B. P.; Cahen, D.; Kronik, L.; Kahn, A. Valence and Conduction Band Densities of States of Metal Halide Perovskites: A Combined Experimental–Theoretical Study. *J. Phys. Chem. Lett.* **2016**, *7*, 2722-2729.

- (30) Wang, R.; Wu, C.; Hu, Y.; Li, J.; Shen, P.; Wang, Q.; Liao, L.; Liu, L.; Duhm, S. CH₃NH₃PbI_{3-x}Cl_x under Different Fabrication Strategies: Electronic Structures and Energy-Level Alignment with an Organic Hole Transport Material. *ACS Appl. Mater. Interfaces* **2017**, *9*, 7859-7865.
- (31) Niesner, D.; Wilhelm, M.; Levchuk, I.; Osvet, A.; Shrestha, S.; Batentschuk, M.; Brabec, C.; Fauster, T. Giant Rashba Splitting in CH₃NH₃PbBr₃ Organic-Inorganic Perovskite. *Phys. Rev. Lett.* **2016**, *117*, 126401.
- (32) Wang, C.; Ecker, B. R.; Wei, H.; Huang, J.; Meng, J. Q.; Gao, Y. Valence Band Dispersion Measurements of Perovskite Single Crystals using Angle-Resolved Photoemission Spectroscopy. *Phys. Chem. Chem. Phys.* **2017**, *19*, 5361-5365.
- (33) Komesu, T.; Huang, X.; Paudel, T. R.; Losovyj, Y. B.; Zhang, X.; Schwier, E. F.; Kojima, Y.; Zheng, M.; Iwasawa, H.; Shimada, K.; Saidaminov, M. I.; Shi, D.; Abdelhady, A. L.; Bakr, O. M.; Dong, S.; Tsymbal, E. Y.; Dowben, P. A. Surface Electronic Structure of Hybrid Organo Lead Bromide Perovskite Single Crystals. *J. Phys. Chem. C* **2016**, *120*, 21710-21715.
- (34) Lee, M.-I.; Barragán, A.; Nair, M. N.; Jacques, V. L. R.; Le Bolloc'h, D.; Fertey, P.; Jemli, K.; Lédée, F.; Trippé-Allard, G.; Deleporte, E.; Taleb-Ibrahimi, A.; Tejada, A. First Determination of the Valence Band Dispersion of CH₃NH₃PbI₃ Hybrid Organic-Inorganic Perovskite. *J. Phys. D* **2017**, *50*, 26LT02.
- (35) Yang, J.-P.; Meissner, M.; Yamaguchi, T.; Zhang, X.-Y.; Ueba, T.; Cheng, L.-W.; Ideta, S.; Tanaka, K.; Zeng, X.-H.; Ueno, N.; Kera, S. Band Dispersion and Hole Effective Mass of Methylammonium Lead Iodide Perovskite. *Solar RRL* **2018**, 1800132.
- (36) Kim, T. W.; Uchida, S.; Matsushita, T.; Cojocaru, L.; Jono, R.; Kimura, K.; Matsubara, D.; Shirai, M.; Ito, K.; Matsumoto, H.; Kondo, T.; Segawa, H. Self-Organized Superlattice and Phase Coexistence inside Thin Film Organometal Halide Perovskite. *Adv. Mater.* **2018**, *30*, 1705230.
- (37) Olthof, S. Research Update: The Electronic Structure of Hybrid Perovskite Layers and Their Energetic Alignment in Devices. *APL Mater.* **2016**, *4*, 091502.
- (38) Emara, J.; Schnier, T.; Pourdavoud, N.; Riedl, T.; Meerholz, K.; Olthof, S. Impact of Film Stoichiometry on the Ionization Energy and Electronic Structure of CH₃NH₃PbI₃ Perovskites. *Adv. Mater.* **2016**, *28*, 553-559.

- (39) Liu, Y.; Yang, Z.; Cui, D.; Ren, X.; Sun, J.; Liu, X.; Zhang, J.; Wei, Q.; Fan, H.; Yu, F.; Zhang, X.; Zhao, C.; Liu, S. Two-Inch-Sized Perovskite $\text{CH}_3\text{NH}_3\text{PbX}_3$ ($X = \text{Cl, Br, I}$) Crystals: Growth and Characterization. *Adv. Mater.* **2015**, *27*, 5176-5183.
- (40) Whitfield, P. S.; Herron, N.; Guise, W. E.; Page, K.; Cheng, Y. Q.; Milas, I.; Crawford, M. K. Structures, Phase Transitions and Tricritical Behavior of the Hybrid Perovskite Methyl Ammonium Lead Iodide. *Sci Rep* **2016**, *6*, 35685.
- (41) Hüfner, S. *Photoelectron Spectroscopy: Principles and Applications*, Springer: Germany, 2003.
- (42) Zhang, P.; Richard, P.; Qian, T.; Xu, Y.-M.; Dai, X.; Ding, H. A Precise Method for Visualizing Dispersive Features in Image Plots. *Rev. Sci. Instrum.* **2011**, *82*, 043712.
- (43) Strocov, V. N. Intrinsic Accuracy in 3-Dimensional Photoemission Band Mapping. *J. Electron. Spectrosc. Relat. Phenom.* **2003**, *130*, 65-78.
- (44) Strocov, V. N.; Claessen, R.; Nicolay, G.; Hüfner, S.; Kimura, A.; Harasawa, A.; Shin, S.; Kakizaki, A.; Nilsson, P. O.; Starnberg, H. I.; Blaha, P. Absolute Band Mapping by Combined Angle-Dependent Very-Low-Energy Electron Diffraction and Photoemission: Application to Cu. *Phys. Rev. Lett.* **1998**, *81*, 4943-4946.
- (45) Emfietzoglou, D.; Kyriakou, I.; Abril, I.; Garcia-Molina, R.; Petsalakis, I. D.; Nikjoo, H.; Pathak, A. Electron Inelastic Mean Free Paths in Biological Matter based on Dielectric Theory and Local-Field Corrections. *Nucl. Instrum. Methods Phys. Res. B* **2009**, *267*, 45-52.
- (46) JBourke, J. D.; Chantler, C. T. Measurements of Electron Inelastic Mean Free Paths in Materials. *Phys. Rev. Lett.* **2010**, *104*, 206601.
- (47) Lindroos, M.; Sahrakorpi, S.; Bansil, A. Matrix Element Effects in Angle-Resolved Photoemission from $\text{Bi}_2\text{Sr}_2\text{CaCu}_2\text{O}_8$: Energy and Polarization Dependencies, Final State Spectrum, Spectral Signatures of specific Transitions, and Related Issues. *Phys. Rev. B* **2002**, *65*.
- (48) Moser, S. An Experimentalist's Guide to the Matrix Element in angle Resolved Photoemission. *J. Electron. Spectros. Relat. Phenomena* **2017**, *214*, 29-52.
- (49) Tong, M. A. V. H. a. S. Y. *Surface Crystallography by LEED*, Springer-Verlag: Berlin, 1979.
- (50) He, Y.; Galli, G. Perovskites for Solar Thermoelectric Applications: A First Principle Study

- of CH₃NH₃AI₃ (A = Pb and Sn). *Chem. Mater.* **2014**, *26*, 5394-5400.
- (51) Shi, T.; Yin, W.-J.; Hong, F.; Zhu, K.; Yan, Y. Unipolar Self-Doping Behavior in Perovskite CH₃NH₃PbBr₃. *Appl. Phys. Lett.* **2015**, *106*, 103902.
- (52) Bonn, M.; Miyata, K.; Hendry, E.; Zhu, X. Y. Role of Dielectric Drag in Polaron Mobility in Lead Halide Perovskites. *ACS Energy Lett.* **2017**, *2*, 2555-2562.
- (53) Frost, J. M. Calculating Polaron Mobility in Halide Perovskites. *Phys. Rev. B* **2017**, *96*.
- (54) Li, B.; Kawakita, Y.; Liu, Y.; Wang, M.; Matsuura, M.; Shibata, K.; Ohira-Kawamura, S.; Yamada, T.; Lin, S.; Nakajima, K.; Liu, S. Polar Rotor Scattering as Atomic-Level Origin of Low Mobility and Thermal Conductivity of Perovskite CH₃NH₃PbI₃. *Nat. Commun.* **2017**, *8*, 16086.
- (55) Zhu, H.; Miyata, K.; Fu, Y.; Wang, J.; Joshi, P. P.; Niesner, D.; Williams, K. W.; Jin, S.; Zhu, X.-Y. Screening in Crystalline Liquids Protects Energetic Carriers in Hybrid Perovskites. *Science* **2016**, *353*, 1409-1413.
- (56) Neukirch, A. J.; Nie, W.; Blancon, J. C.; Appavoo, K.; Tsai, H.; Sfeir, M. Y.; Katan, C.; Pedesseau, L.; Even, J.; Crochet, J. J.; Gupta, G.; Mohite, A. D.; Tretiak, S. Polaron Stabilization by Cooperative Lattice Distortion and Cation Rotations in Hybrid Perovskite Materials. *Nano Lett.* **2016**, *16*, 3809-3816.
- (57) Bocquet, F. C.; Giovanelli, L.; Amsalem, P.; Petaccia, L.; Topwal, D.; Gorovikov, S.; Abel, M.; Koch, N.; Porte, L.; Goldoni, A.; Themlin, J. M. Final-State Diffraction Effects in Angle-Resolved Photoemission at an Organic-Metal Interface. *Phys. Rev. B* **2011**, *84*.
- (58) Giovanelli, L.; Bocquet, F. C.; Amsalem, P.; Lee, H. L.; Abel, M.; Clair, S.; Koudia, M.; Faury, T.; Petaccia, L.; Topwal, D.; Salomon, E.; Angot, T.; Cafolla, A. A.; Koch, N.; Porte, L.; Goldoni, A.; Themlin, J. M. Interpretation of Valence Band Photoemission Spectra at Organic-Metal Interfaces. *Phys. Rev. B* **2013**, *87*.
- (59) Giovanelli, L.; Amsalem, P.; Angot, T.; Petaccia, L.; Gorovikov, S.; Porte, L.; Goldoni, A.; Themlin, J. M. Valence Band Photoemission from the Zn-phthalocyanine/Ag(110) Interface: Charge transfer and Scattering of Substrate Photoelectrons. *Phys. Rev. B* **2010**, *82*.
- (60) Zu, F.-S.; Amsalem, P.; Salzmann, I.; Wang, R.-B.; Ralaiarisoa, M.; Kowarik, S.; Duhm, S.; Koch, N. Impact of White Light Illumination on the Electronic and Chemical Structures of Mixed Halide and Single Crystal Perovskites. *Adv. Optical Mater.* **2017**, *5*, 1700139-n/a.

- (61) Ralaifarisoa, M.; Salzmann, I.; Zu, F.-S.; Koch, N. Effect of Water, Oxygen, and Air Exposure on CH₃NH₃PbI_{3-x}Cl_x Perovskite Surface Electronic Properties. *Adv. Electron. Mater.* **2018**, *4*, 1800307.
- (62) Zhang, W.; Pathak, S.; Sakai, N.; Stergiopoulos, T.; Nayak, P. K.; Noel, N. K.; Haghighirad, A. A.; Burlakov, V. M.; deQuilettes, D. W.; Sadhanala, A.; Li, W.; Wang, L.; Ginger, D. S.; Friend, R. H.; Snaith, H. J. Enhanced Optoelectronic Quality of Perovskite Thin Films with Hypophosphorous Acid for Planar Heterojunction Solar Cells. *Nat. Commun.* **2015**, *6*, 10030.
- (63) Sueyoshi, T.; Fukagawa, H.; Ono, M.; Kera, S.; Ueno, N. Low-Density Band-Gap States in Pentacene Thin Films Probed with Ultrahigh-Sensitivity Ultraviolet Photoelectron Spectroscopy. *Appl. Phys. Lett.* **2009**, *95*, 183303.
- (64) Lu, M. C.; Wang, R. B.; Yang, A.; Duhm, S. Pentacene on Au(1 1 1), Ag(1 1 1) and Cu(1 1 1): From Physisorption to Chemisorption. *J. Phys. Condens. Matter.* **2016**, *28*, 094005.
- (65) Mom, R. V.; Hahn, C.; Jacobse, L.; Juurlink, L. B. F. LEED Analysis of a Nickel Cylindrical Single Crystal. *Surf Sci.* **2013**, *613*, 15-20.
- (66) Kresse, G.; Furthmüller, J. Efficient Iterative Schemes for Ab Initio Total-Energy Calculations using a Plane-Wave Basis Set. *Phys. Rev. B* **1996**, *54*, 11169-11186.
- (67) Heyd, J.; Scuseria, G. E.; Ernzerhof, M. Hybrid Functionals based on a Screened Coulomb Potential. *J. Chem. Phys.* **2003**, *118*, 8207-8215.
- (68) Egger, D. A.; Kronik, L. Role of Dispersive Interactions in Determining Structural Properties of Organic–Inorganic Halide Perovskites: Insights from First-Principles Calculations. *J. Phys. Chem. Lett.* **2014**, *5*, 2728-2733.